Available online at www.sciencedirect.com
ScienceDirect
International Journal of Heat and Mass Transfer 50 (2007) 3977–3989
International Journal of HEAT and MASS TRANSFER
www.elsevier.com/locate/ijhmt

Effects of temperature and disorder on thermal boundary conductance at solid–solid interfaces: Nonequilibrium molecular dynamics simulations

Robert J. Stevens [a,*], Leonid V. Zhigilei [b], Pamela M. Norris [c]

[a] Department of Mechanical Engineering, Rochester Institute of Technology, Rochester, NY 14623, USA
[b] Department of Material Science and Engineering, University of Virginia, Charlottesville, VA 22904, USA
[c] Department of Mechanical and Aerospace Engineering, University of Virginia, Charlottesville, VA 22904, USA

Received 29 June 2006; received in revised form 24 January 2007
Available online 2 April 2007

Abstract

Thermal transport across interfaces is becoming increasingly important with the advent of nanostructures and nanocomposite materials. A nonequilibrium molecular dynamics (NEMD) approach is developed to investigate thermal transport across solid–solid interfaces. Thermal boundary conductance is calculated for a range of mismatched interfaces and compared to the diffuse mismatch model (DMM). The interfacial conductance decreased with increasing mismatch, as expected. The DMM fits the NEMD results well for poorly matched interfaces at a temperature approximately half of the melting temperature of the material, but it underpredicts the conductance for highly matched interfaces. One of the key findings of this study is that there is a significant interfacial thermal transport dependence on temperature in the NEMD simulations, which is not accounted for by the mismatch models where only elastic scattering is considered. For large lattice mismatches that resulted in numerous defects at the interface, the thermal interfacial conductance dramatically decreased for interfaces with similar vibrational density of states. The presence of the defects had a minimal impact on the thermal transport for highly mismatched interfaces. Interface mixing improves thermal transport by nearly a factor of two for mixing depths of 20 atomic planes for highly mismatched interfaces.

Keywords: Thermal boundary resistance; Molecular dynamics simulations; Interfaces; Nanocomposites; Thermal boundary conductance

1. Introduction

With the advent of nanoscale devices and structures, we are having to increasingly make the shift from macroscopic thermal transport models to models and theories based on microscopic principles [1,2]. This is particularly the case with the growing interest in nanocomposites and superlattices [3]. In such structures, interfaces can dominate the overall thermal resistance compared to the thermal resistances associated with the constituent materials. The interface thermal resistance, often referred to as thermal boundary resistance, R_{BD}, or Kapitza resistance, can vary widely depending on both the microstructure of the interface and the materials utilized. Thermal boundary resistance creates a temperature drop, ΔT, across an interface between two different materials when a heat flux is applied. The inverse of thermal boundary resistance is known as Kapitza conductance, h_{BD}, or thermal boundary conductance. The heat flux, q'', across an interface can be expressed by the following equation:

$$q'' = h_{BD}\Delta T = \frac{1}{R_{BD}}\Delta T. \quad (1)$$

Thermal resistances for solid–solid interfaces, R_{BD}, are typically 10^{-9}–10^{-7} m^2 K/W at room temperatures, which are not to be confused with contact resistances. Contact

* Corresponding author. Tel.: +1 585 475 2153; fax: +1 585 475 7710.
E-mail address: rjseme@rit.edu (R.J. Stevens).

0017-9310/$ - see front matter © 2007 Elsevier Ltd. All rights reserved.
doi:10.1016/j.ijheatmasstransfer.2007.01.040

Nomenclature

a	lattice parameter
A	single measurement
c	phonon propagation speed
C	scaling factor
C_p	specific heat
$DELTAE$	energy added to bath atoms per time step
E	energy
F_{ij}	force acting on atom i due to atom j
g	phonon density of state per unit volume
$\hbar$	Planck's constant
h_{BD}	Kapitza or thermal boundary conductance
k	number of atoms in regions of interest
k_B	Boltzmann constant
l	indexing integer
m	particle mass
M	# of measurements made
n	Bose–Einstein distribution function or atomic number density
N	number of particles in bath
q''	heat flux across an interface
r	distance
r_c	cutoff distance
R_{ij}	distance between atoms i and j
R_θ	Debyte temperature ratio
SE	percentage standard error
t	time
T	temperature
U	interatomic potential function
u_{total}	energy per unit volume of a subsystem
$v, \vec{V}$	particle velocity
VAF	velocity autocorrelation function
XL, YL	crystal width in x- and y-directions
$\langle\ \rangle$	expected value

Greek symbols

α	transmission coefficient incident on an interface
Δt	simulation time step
ε	energy parameter for the LJ potential
γ	phonon incidence angle or scaling factor for bath
θ_D	Debye temperature
ρ	density
σ	lattice parameter for Lennard-Jones potential or statistical error
τ	autocorrelation time
ω	angular frequency of phonon

Subscripts

0	initial
1	side one of interface or first decay process
2	side two of interface or second decay process
A	side A of interface
AA	atom of type A to atom of type A
AB	atom of type A to atom of type B
B	side B of interface
BB	atom of type B to atom of type B
b	bath atoms
D	Debye
E	due to elastic scattering
eff	effective
h_{BD}	thermal boundary conductance
i	interface or indexing integer
I	due to inelastic scattering
j	phonon polarization
l	longitudinal polarization
LJ	Lennard-Jones potential
max	maximum sustained phonon angular frequency of material
t	total or transverse polarization

resistances, which are associated with poor mechanical connection between two materials, are typically one or more orders of magnitude larger than thermal boundary resistances. Although the interface resistances are small, they become critical in structures where there are numerous interfaces. This is especially the case for devices with multiple interfaces such as superlattices [4] and ultra large scale integrated circuits. Specific applications where interface resistances are currently being considered include thermoelectrics [5–11], thin-film high temperature superconductors [12–15], vertical cavity surface emitting lasers [16], and optical data storage media [17]. As nanotechnologies take more of a foothold, more applications are sure to follow.

The primary energy carriers in semiconductors and dielectric materials are acoustic phonons. Consequently, the h_{BD} of dissimilar dielectric materials is often reduced because of the scattering of phonons at the interface. There have been several theoretical models developed to estimate the h_{BD} of interfaces. The first of these theories is the acoustic mismatch model (AMM) developed in 1952 by Khalatnikov for liquid helium–solid interface [18] and later altered by Little for interfaces of dissimilar solids at low temperatures [19]. This model assumes that each solid can be treated as a continuum with a perfect interface. The incident phonons are treated as plane waves, for which transmission and reflection probabilities are calculated, and there is no scattering at the interface. A more recent model called the diffuse mismatch model (DMM) was developed and is generally more applicable at higher temperatures. This model assumes complete diffuse scattering at the interface [20]. The transmission

probability is then related to the density of phonon states on both sides of the interface. Diffuse scattering is more important at higher temperatures and for non-perfect interfaces. Experiments indicate that the DMM does not fully capture all the thermal transport mechanisms occurring at the interfaces [21–23].

Early computational efforts utilized lattice-dynamics calculations to numerically determine the h_{BD} under the assumptions of harmonic oscillations and elastic scattering [24–28]. Molecular dynamics simulations (MDS) began to be used as a means of understanding h_{BD} and investigating transport in more realistic anharmonic crystal models, while having systematic control over interfaces, which is difficult to do experimentally. One of the earliest of these studies by Picket et al. was developed to better understand the low thermal resistance of chemical vapor deposited diamond films [29]. Maiti et al. ran MDS to gain insight on the h_{BD} across Si grain boundaries [30]. Using MDS Daly et al. examined thermal conductivity of superlattices and found that interfacial roughness of a few monolayers resulted in a significant decrease in the h_{BD} [31]. Schelling et al. utilized MDS to determine phonon transmission coefficients as a function of phonon frequency using the Stillinger–Weber potential [32]. They showed good agreement between their model and AMM results for low frequency phonons, but found large deviations for the high-energy phonons that dominate the thermal energy transport at room temperature. Liang and Sun [33,34] and Twu and Ho [32] have done some preliminary work on the impact of interface disorder Choi and Maruyama conducted MDS on epitaxial interfaces [35].

This study develops one of the most comprehensive series of molecular dynamics simulations to gain insight into thermal transport at interfaces between dissimilar materials. The results are compared to the DMM, which is the model typically used for engineering purposes for interface transport at room temperature. To date, there has not been a direct comparison between the DMM and NEMD simulations. The relationships between the thermal transport, temperature, and interface disorder are also considered, which have had limited attention in previous works.

2. Molecular dynamics simulation method

There are two MDS approaches which can be used to conduct thermal boundary resistance simulations. The first approach is to create a temperature gradient across an interface by either adding a constant amount of energy to a thermal bath of atoms on one side of the structure while removing the same amount on the other side or by holding the thermal baths of atoms at the two ends of the simulation structure at some desired temperatures. Once steady state in the system is reached, Fourier's law is applied. This technique is often called the direct method or nonequilibrium molecular dynamics (NEMD). The NEMD approach is described by Chantrenne and Barrat for determining thermal conductivity in nanostructured materials [36]. This approach is directly analogous to the way we would experimentally measure thermal conductivity in macroscopic materials.

The second approach is an equilibrium approach that makes use of the Green–Kubo (GK) method. At equilibrium, the thermal current at any particular location will fluctuate about zero. The time between fluctuations is then related to thermal transport properties of the material. The GK or equilibrium approach is described in detail by Frenkel and Smith [37] and McQuarrie [38]. It is not clear whether the GK approach is suitable for determining thermal properties of inhomogeneous systems (grain boundaries, superlattices, and interfaces). Schelling et al. compared the two techniques for measuring thermal conductivity in Si and found little difference between the two approaches and good agreement with experimental values [39]. The NEMD approach is employed in this work and applied to a range of interfaces.

2.1. NEMD approach

The NEMD approach taken in this study is to apply a temperature gradient across an interface of two materials (A and B) as shown in Fig. 1. This leads to a temperature drop at the interface, which can then be used to calculate the thermal boundary conductance using Eq. (1). A simulation consists of scaling the initial velocities of the system to achieve a desired temperature [37]. The crystal is then allowed to equilibrate. An energy flux is then applied and the system is allowed to reach a steady state condition. The system is then held in the steady state condition for several time steps to get a statistical measure of temperature and to reduce uncertainties in the measurement of h_{BD}.

Periodic boundary conditions are used in x- and y-directions as defined in Fig. 1. This simulates an infinitely large slab in these directions. Both fixed and periodic boundary

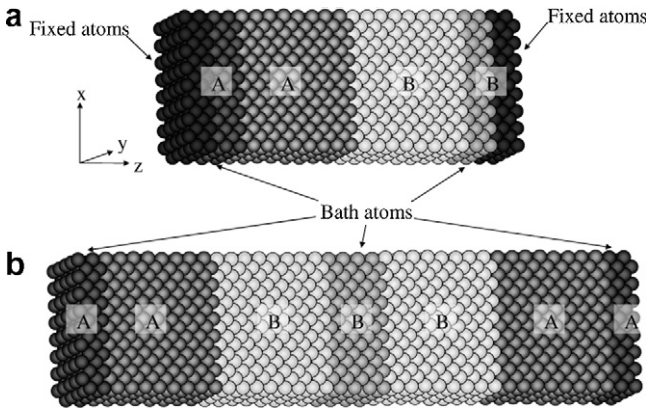

Fig. 1. Comparison of two boundary conditions considered: (a) fixed boundary conditions in the z-direction. The edge of the structure consists of four atomic planes of fixed "wall" atoms (black) and four atomic planes used for the hot and cold bath atoms (dark grey and light grey). Typically, six atoms were used in the bath, but only four are shown here, (b) periodic boundary conditions, which simulates an infinite number of repeating interfaces in the z-direction, the heating and cooling bath atoms generally consisted of six atomic planes (dark grey and light grey).

conditions are considered in the z-direction as shown in Fig. 1a and b, respectively. For the fixed boundary condition case, four atomic planes on the far edges of the simulation cell were fixed, which simulates infinite adiabatic walls. These wall atoms are shown in black in Fig. 1a. Next to the fixed walls are the hot and cold baths, which typically consisted of six atomic planes. Alternatively, periodic conditions are used in z-direction (normal to the interface), as shown in Fig. 1b, simulating an infinite array of parallel interfaces with heating and cooling zones located in the middle of crystallites A and B, respectively. Six atomic planes were typically used for the heating and cooling baths, as described in more detail below. Both the fixed and periodic boundary condition approaches have been used to measure the thermal conductivity and h_{BD} [34,36,40–43]. In this study, it was found that both the fixed and periodic boundary conditions produce results within the uncertainty of the NEMD experiments as long as the crystal size was chosen appropriately. The crystal size was chosen by increasing the size in all three dimensions until there was no statistically significant size effect on the results of the simulations. The crystal size typically used in this study had widths of 10 atomic planes and a length of 80 atomic planes.

The pair-wise Lennard-Jones (LJ) potential was used to describe the interatomic interaction on both sides of the system. To minimize computational effort, the interatomic potential function was terminated at 2.5σ, where σ is the LJ lattice parameter, and a cutoff function suggested by Stoddard and Ford [44] was used to ensure that the potential and forces are continuous at the cutoff distance of $r_c = 2.5\sigma$:

$$U = \sum_{i=1}^{N}\sum_{j>i}^{N} 4\varepsilon\left\{\left[\left(\frac{\sigma}{R_{ij}}\right)^{12} - \left(\frac{\sigma}{R_{ij}}\right)^{6}\right] + \left[6\left(\frac{\sigma}{r_c}\right)^{12} - 3\left(\frac{\sigma}{r_c}\right)^{6}\right](r/r_c)^2 - 7\left(\frac{\sigma}{r_c}\right)^{12} + 4\left(\frac{\sigma}{r_c}\right)^{6}\right\} \quad (2)$$

where R_{ij} is distance between atoms i and j, and ε and σ are parameters defining the energy and length-scales of the potential function.

Parameters for the interaction between atoms of different types were defined using the Lorentz–Berthelot rules, $\varepsilon_{AB} = \sqrt{\varepsilon_{AA}\varepsilon_{BB}}$ and $\sigma_{AB} = (\sigma_{AA} + \sigma_{BB})/2$ [45]. Although the LJ potential provides a realistic description of only a limited number of real systems (inert gases, van der Waals interaction in molecular systems), it is often used to model other systems when general effects rather than properties of a specific material are of interest. Since this study is primarily interested in the fundamental mechanisms of thermal transport across solid–solid interfaces and not h_{BD} of a particular interface, the LJ potential was used to account for the general anharmonic nature of real materials, which has not been accounted for in earlier harmonic models. In addition, because the intent of this work is to be general, NEMD h_{BD} results are presented in non-dimensional units, otherwise known as LJ reduced units,

$$r^* = r/\sigma, \quad E^* = E/\varepsilon, \quad T^* = k_B T/\varepsilon,$$
$$t^* = t \times \sqrt{\varepsilon/(m\sigma^2)}, \quad \omega^* = \omega \times \sqrt{(m\sigma^2)}/\varepsilon, \quad h^*_{BD} = h_{BD}\frac{m^{1/2}\sigma^3}{\varepsilon^{1/2}k_B} \quad (3)$$

where m, σ, and ε are mass and the two LJ parameters of side A atoms and E, T, t, and ω are energy, temperature, time, and angular frequency, respectively. The "*" is not used in the remaining text and reduced units are implied unless specified otherwise.

Most interfaces were generated by starting with an fcc structure and assigning atoms to a particular atom type defined by the three parameters, m, σ, and ε. This allows a wide range of interface mismatches to be generated. In all cases, the interfaces were oriented along the (0 0 1) crystallographic plane. The equations of motion for all atoms in the system were integrated using the Nordsieck–Gear fifth-order predictor–corrector algorithm [45].

There are a few options for creating a steady state temperature gradient across the interfaces. The general approach that has been used by several groups to simulate thermal conductivity and h_{BD} is to define a bath of atoms on both sides located far away from the interface or area of interest [36,40,41,43,46,47]. Energy is then deposited or removed at each time step in these baths. As in the case of Fig. 1, the dark grey atoms are the heated bath, while the grey atoms are the cooled bath.

The simplest approach to regulating the baths is to define a desired heat flux and to add energy to the hot bath and remove the same amount of energy from the cold bath at each time step. In this case, the fixed energy added and removed per time step is

$$DELTAE = q'' \cdot XL \cdot YL \cdot \Delta t \quad (4)$$

where XL, YL are the dimensions of the computational cell in the x- and y-directions, and Δt is the simulation time step. The fixed amount of energy is added by scaling the velocity of each atom in the baths using a technique developed by Ikeshoji and Hafkjold [46], which ensures conservation of momentum. Ikeshoji and Hafskjold assume that a single type of atom is used in the bath. One of the major disadvantages of this approach is that the final steady state temperature across the structure is unknown at the beginning of the simulation making it difficult to change the interface temperature systematically. In addition, at low temperatures errors can also occur due to the generation of imaginary scaling factors.

The second set of approaches maintains the temperature of the baths and avoids the problems associated with a constant heat flux approach. Initially the two baths are heated to the desired temperatures by scaling the velocities using a modified Ikeshoji and Hafkjold method where instead of having a constant heat flux, the energy added is defined as

$$DELTAE = \gamma\frac{3}{2}k_B N(T_0 - T_b) \quad (5)$$

where T_b is the current bath temperature and is defined as

$$T_b = \sum_{i=1}^{N} \frac{m_i v_i^2}{3k_B N} \tag{6}$$

in accordance with the equipartition principle, and γ is a scaling factor inversely related to the time of temperature relaxation of the bath ($\ll 1$). N, m, v, and k_B are the number of particles in the bath, the mass and velocity of an atom, and the Boltzmann constant. Once the baths reach the desired temperature, the temperatures are then controlled by either a simple velocity scaling or by the Gaussian thermostat method [48]. Both methods were utilized in this work and it was found that there were negligible differences in the two approaches.

During the time when the system is approaching a steady state condition, which is typically on the order of 10^6 time steps for a large system, the total pressure is maintained at zero using the Berendsen barostat scheme [49]. Pressure control was terminated shortly before the beginning of the data collection for h_{BD}.

2.2. Calculating thermal boundary conductance

To determine the h_{BD} for a particular interface using the NEMD approach, the heat flux, q'', and temperature drop, ΔT, across the interface must be measured at the steady state condition. The steady state average q'' can be assumed to be the total energy added to the hot bath divided by the cross-sectional area of the cell and the total time during the measurement:

$$q'' = \frac{1}{XL \cdot YL \cdot \Delta t \cdot N_t} \sum_{N_t} DELTAE \tag{7}$$

where N_t is the total number of simulated time steps.

Lukes et al., when conducting thermal conductivity simulations, found that the heat flux calculated using Eq. (7) differed slightly from the heat flux calculated using equations of Irving and Kirkwood [50]. They attributed this error to small nonzero fluxes that occur in the x- and y-directions. But under the periodic boundary conditions, these fluxes should never leave the system and energy should be conserved. To verify Eq. (7), the actual energy flux across the interface in NEMD can be calculated by considering the work per unit time exerted by atoms from one side of the interface on the ones on the other side of the interface [51]:

$$q'' = \frac{1}{XL \cdot YL \cdot N_t} \sum_{N_t} \sum_{i \in side} \sum_{j \in sideA} \vec{F}_{ij} \vec{v}_i \tag{8}$$

where $\vec{F}_{ij}$ is the force acting on atom i due to atom j, and v_i is the velocity of atom i.

In all boundary condition and temperature control cases described above, there was negligible difference between Eqs. (7) and (8) when averaged over many time steps once the steady state was reached. Eq. (8) is used to calculate the steady state fluxes throughout the remaining portion of this text and is normally averaged over several million time steps.

The temperature drop across the interface is determined by first calculating the temperatures for each atomic plane parallel to the interface using the same Eq. (6) as for the bath atoms, where N in this case is the number of atoms per plane. Although a nonequilibrium approach is used, local thermal equilibrium and hence local temperature can still be defined when data are averaged over many time steps and for moderate heat fluxes. Typically, temperature drops across the entire structure are held to 0.05. Thermal equilibrium is characterized by the Maxwell–Boltzmann velocity distribution. To confirm the local thermal equilibrium, the velocity distributions of atoms belonging to particular atomic planes are calculated and compared to the Maxwell–Boltzmann distributions. Fig. 2 shows the velocity distributions for a typical simulation for an atomic plane in the middle of side A and adjacent to the interface on side A at the steady state condition. The distributions are described well by the Maxwell–Boltzmann distribution

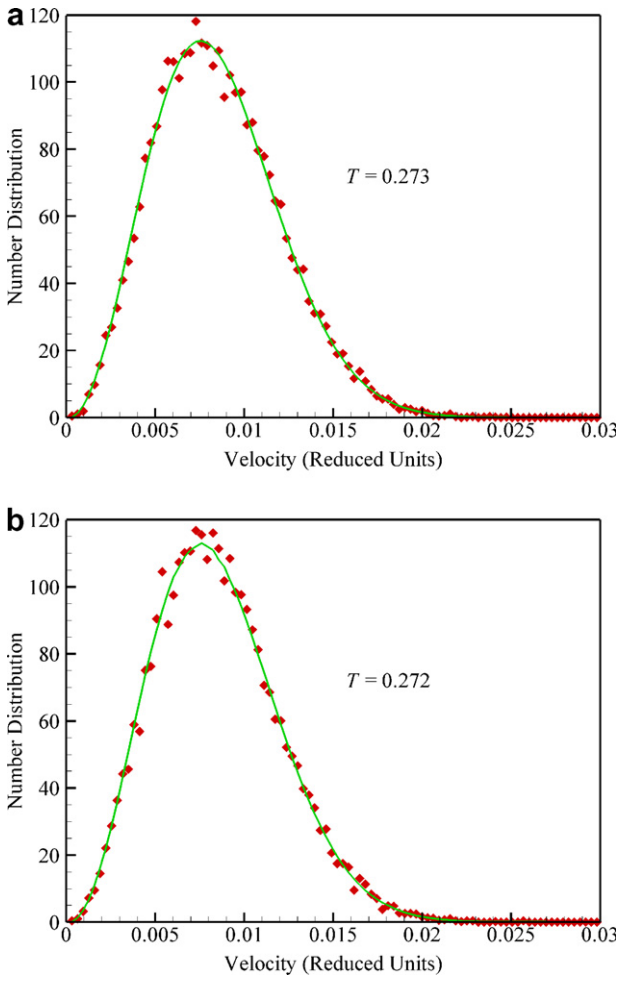

Fig. 2. Velocity distributions for a typical simulation at steady state conditions compared to the Maxwell–Boltzmann distribution functions at the average atomic plane temperature. The temperatures used to calculate the distribution are the average temperatures for the atomic plane during for the simulation. Distributions are based on sampling all atoms in a plane at 20,000 uncorrelated times: (a) distribution for an atomic plane in the middle of side A, and (b) distribution for an atomic plane immediately adjacent to the interface on side A.

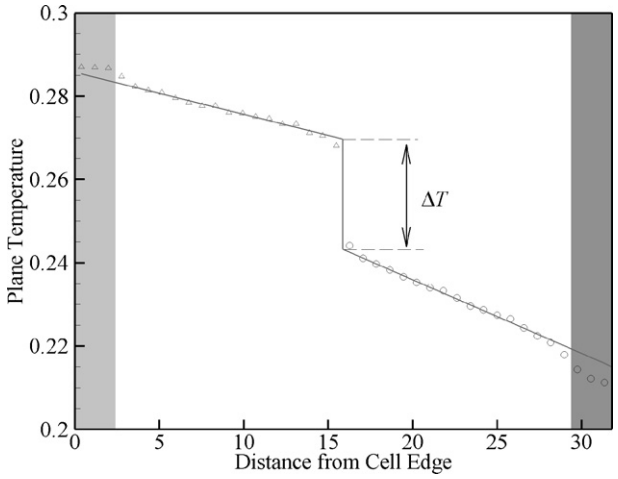

Fig. 3. Typical temperature profile observed in a NEMD simulation of thermal boundary resistance. Triangles are for atoms of type A and circles are for atoms of type B. Areas in the shaded regions are the atomic planes that are heated and cooled, respectively. The figure shows how ΔT is defined for h_{BD} calculation.

functions at the respective plane temperatures, indicating that the local thermal equilibrium assumption is valid.

A typical temperature distribution observed in the steady state regime is shown in Fig. 3. There is a temperature drop at the interface as expected. The thermal boundary resistance is calculated by first performing a linear least squares fit to the temperature distribution for both parts of the system and then looking at the difference between the two linear fits at the interface. The two atomic planes on either side of the interface and adjacent to the heating/cooling baths were not included in the fitting. This strategy, similar to the one used by Twu and Ho [34], is true to the way the continuum Fourier model would be applied with an interface boundary condition.

2.3. Error and uncertainty analysis

As with all measurements, there will be errors in the measured ΔT and q'' and therefore errors in h_{BD}. NEMD errors can include both systematic and statistical errors [52]. Systematic errors are due to the finite-size effects, interaction cutoff, and numerical integration round off. For a discussion on the size effects and numerical errors, see Stevens [53]. Interaction cutoff error is not relevant to this study since the purpose is not to examine a specific material system but to elucidate general trends in the behavior of interfaces.

Statistical errors are due to random uncorrelated fluctuations in the data sampling. The statistical error in h_{BD} is given by

$$\sigma_{h_{BD}} = \sqrt{\sigma^2_{\langle q''\rangle}\left(\frac{\partial h_{BD}}{\partial\langle q''\rangle}\right)^2 + \sigma^2_{\langle \Delta T\rangle}\left(\frac{\partial h_{BD}}{\partial\langle \Delta T\rangle}\right)^2} = \sqrt{\sigma^2_{\langle q''\rangle}\left(\frac{1}{\langle \Delta T\rangle}\right)^2 + \sigma^2_{\Delta T}\left(\frac{\langle q''\rangle}{\langle \Delta T\rangle^2}\right)^2} \quad (9)$$

where σ^2 is the variance for the expected heat flux or interface temperature drop. The expected value of any property A, $\langle A\rangle$, such as ΔT or q'', can be determined by

$$\langle A\rangle = \frac{1}{M}\sum_{i=1}^{M} A_i \quad (10)$$

where A_i is a single measurement and M is the number of measurements made. The expected variance of $\langle A\rangle$ can be determined by

$$\sigma^2_{\langle A\rangle} = \frac{\left[\frac{1}{M-1}\sum_{i=1}^{M}(A_i - \langle A\rangle)^2\right]}{M} \quad (11)$$

where A_i are completely uncorrelated measurements. To ensure measurements are uncorrelated, measurements of A_i should be made at time steps greater than the correlation time. The percentage standard error in the estimate given by Eq. (9) is then

$$SE = \left|\frac{\sigma_{\langle A\rangle}}{\langle A\rangle}\right|. \quad (12)$$

Consider an interface with two materials that have identical LJ parameters and a mass ratio of 1:25 where data was collected over five million time steps. The heat flux was sampled by averaging Eq. (8) for each 5000 time steps, giving a sample size of 1000. The time between samples is significantly longer than the correlation time, which is on the order of 100 time steps. For most cases, the SE in the heat flux based on Eq. (12) was less than 1%.

The standard deviation of ΔT is

$$\sigma_{\Delta T} = \sqrt{\sigma^2_{T_A}\left(\frac{\partial \Delta T}{\partial T_A}\right) + \sigma^2_{T_B}\left(\frac{\partial \Delta T}{\partial T_B}\right)} = \sqrt{\sigma^2_{T_A} + \sigma^2_{T_B}} \quad (13)$$

where $\sigma^2_{T_A}$ and $\sigma^2_{T_B}$ are the variances associated with the least squares fits for sides A and B, respectively. The standard error for ΔT in most simulation runs was typically less than 5%. Therefore, the total standard error in h_{BD} based on Eq. (9) is typically 6% or less. To verify this uncertainty, five separate simulations were conducted on the same interface and the standard error in h_{BD} was determined for this sample of five observations to be 8% of the average h_{BD}. Therefore, it is reasonable to assume that the statistical uncertainty for all simulations is approximately 6–8%.

3. Atomically perfect interfaces

Using the NEMD tools presented above, the effects of temperature and vibrational mismatch between two different materials on thermal transport at an interface can be determined without the introduction of other possible influences such as interface defects, strain, varying interatomic potentials, or electron scattering, which is nearly impossible to do experimentally.

The simplest and most straightforward way to vary the vibration states on either side of an interface is to vary the mass ratio of A and B atoms while holding the LJ energy, ε, and lattice, σ, parameters constant. Changing the mass of

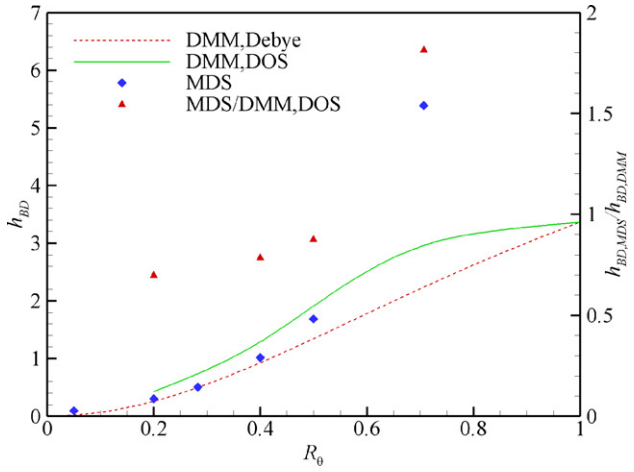

Fig. 4. Thermal boundary conductance as a function of R_θ for the two materials forming an atomically perfect interface.

the atoms directly affects the vibrational (phonon) spectrum of the crystal, which gives the flexibility to investigate the effects of phonon frequency mismatch on h_{BD}. Frequencies of atomic vibrations are inversely proportional to $m^{1/2}$, so that the ratio of Debye temperatures, R_θ, for any two simulated atom types is equal to $(m_A/m_B)^{1/2}$. Thus R_θ is a qualitative indicator of how well the phonon spectra of the two sides overlap.

The mass ratios for the interfaces considered were $m_A/m_B = 0.5$, 0.25, 0.16, 0.08, and 0.04 resulting in cutoff frequency ratio or R_θ values of 0.707, 0.5, 0.4, 0.28, and 0.2, respectively. The diamonds in Fig. 4 show how h_{BD} varies with R_θ at a reduced temperature of the interface equal to 0.25 for atomically perfect interfaces. To give a qualitative sense of what a temperature of 0.25 is, note that for LJ solids the melting temperature is approximately 0.5. Note that h_{BD} is given in reduced units based on the side with the minimum cutoff frequency. There is more than one order of magnitude difference between h_{BD} for the sample interfaces simulated. The wide range in the results is consistent with the DMM for interfaces with Debye ratios less than 0.6, but has yet to be observed experimentally at high temperatures. The dashed and solid curves shown in Fig. 4 represent the results of computations with the DMM under two different scenarios, one assuming a DOS given by the Debye model, and the other assuming a more realistic DOS determined from MDS. Detailed discussion of the calculations performed with the DMM is given below.

3.1. Comparison with DMM

To compare the NEMD results with the DMM and real interfaces, physical properties must be extracted for the simulated materials. Consider the DMM [20,23],

$$h_{BD,1} = \frac{1}{2}\sum_j \frac{\partial}{\partial T}\int_0^{\pi/2}\int_0^{\varpi_{max}} g_{1,j}(\omega)n(\omega,T)\hbar\omega c_{1,j}\alpha_{1,j}(\gamma,j,\omega) \times \cos(\gamma)\sin(\gamma)\,d\omega\,d\gamma \quad (14)$$

where g is the phonon density of states, n is the Bose–Einstein distribution function, $\hbar$ is the Planck's constant, ω is the phonon angular frequency, c is the phonon propagation speed, α is the transmission probability, γ is the incident angle, and j is the phonon polarization. For the DMM, it is assumed that the phonon transmission probability, α, is independent of the incidence angle. It is also assumed that the phonon propagation speeds, $c_{1,j}$, are independent of direction. This last condition is really only valid for highly polycrystalline or amorphous materials, but in the MDS case the assumption will be made that the propagation speed is approximately equivalent to the speed of a traveling wave in the [1 0 0] direction for each polarization. With these assumptions Eq. (14) reduces to

$$h_{BD,1} = \frac{1}{4}\sum_j \frac{\partial}{\partial T}\int_0^{\varpi_{max}} g_{1,j}(\omega)n(\omega,T)\hbar\omega c_{1,j}\alpha(j,\omega)\,d\omega. \quad (15)$$

Also, in the classical limit, the vibrational states will be occupied in a linear fashion with respect to temperature, which is the functional form of the Bose–Einstein distribution in the high temperature limit. In order to apply Eq. (15) to the MDS, $g_{1,j}(\omega)n(\omega,T)$, $c_{1,j}$, and α must be specified. These can be determined by two different methods. The first is to assume a Debye solid, so that the vibrational density of states and transmission coefficient will be dependent on the phonon propagation speeds. This approach is simpler, allows the separation of longitudinal and transverse polarizations, and is in the same spirit as much of the past experimental work. The second approach involves measuring the vibrational density of states and measuring the propagation speed for each simulated crystal. These values are then used to calculate the transmission coefficient and h_{BD}.

3.1.1. Debye approximation

The Debye approximation assumes the phonon velocity to be constant for each polarization type. For Debye solids, the density of states is [54]

$$g_j(\omega) = \frac{\omega_j^2}{2\pi^2 c_j^3}. \quad (16)$$

In the classical limit and under the harmonic approximation the heat capacity for each polarization, $C_{p,j}$, can be found by differentiating the thermal energy associated with each polarization as follows:

$$C_{p,j} = \frac{d}{dT}\int_0^{\omega_{D,j}} g_{1,j}(\omega)n(\omega,T)\hbar\omega\,d\omega = \int_0^{\omega_{D,j}} \frac{C\omega^2}{2\pi^2 c_j^3}\hbar\omega\,d\omega = \frac{C\hbar\omega_{D,j}^4}{8\pi^2 c_j^3} \approx nk_B \quad (17)$$

where $\omega_{D,j}$, n, and C are the Debye frequency of polarization j, the number density, and the proportionality constant. For LJ solids, as will be discussed below, the energy associated with each degree of freedom in the

crystal is $\sim(1.1)nk_B$ due to anharmonicity of the crystal, so the proportionality constant is:

$$C = (1.1)\frac{8\pi^2 c_j^3 k_B n}{\omega_{D,j}^4 \hbar}. \tag{18}$$

The Debye solid transmission coefficient is [23]

$$\alpha_A(\omega) = \frac{\sum_j c_{B,j}^{-2}}{\sum_j c_{B,j}^{-2} + c_{A,j}^{-2}}. \tag{19}$$

Substituting Eqs. (17)–(19) into Eq. (15) leads to

$$h_{BD,1} \approx (1.1)\frac{nk_B}{4}\sum_j \frac{c_{1,j}c_{2,j}^{-2}\omega_{max,j}^4}{(c_{1,j}^{-2}+c_{2,j}^{-2})\omega_{D,1,j}^4} \tag{20}$$

where $\omega_{max,j}$ is the smallest of the two cutoff frequencies at both sides of the interface for vibrational polarization j and $\omega_{D,1,j}$ is the Debye frequency for side one and polarization j. Consider the selection of side one such that $\omega_{D,1,j} < \omega_{D,2,j}$, which is the same as $\theta_{D,1} < \theta_{D,2}$. For LJ solids this can be expressed as:

$$\frac{1}{\sigma_1}\left(\frac{\varepsilon_1}{m_1}\right)^{1/2} < \frac{1}{\sigma_2}\left(\frac{\varepsilon_2}{m_2}\right)^{1/2}. \tag{21}$$

For the case of Eq. (21), $\omega_{max,j} = \omega_{D,1,j}$, so Eq. (20) reduces to

$$h_{BD} = (1.1)\frac{nk_B}{4}\sum_j \frac{c_{1,j}c_{2,j}^{-2}}{(c_{1,j}^{-2}+c_{2,j}^{-2})}. \tag{22}$$

For fcc LJ solids with a cutoff distance of 2.5σ, the number density is

$$n = \frac{4}{a^3} = \frac{4}{(\sqrt{2}(1.09574\sigma))^3} = \frac{1.075}{\sigma^3}. \tag{23}$$

There are two options for determining the propagation velocities for both the longitudinal and transverse polarizations. The first is to use the elastic stiffness constants or moduli of elasticity. For propagating elastic waves in the [1 0 0] direction the longitudinal and transverse velocities are [54]:

$$c_l = (C_{11}/\rho)^{1/2} \tag{24}$$

$$c_t = (C_{44}/\rho)^{1/2} \tag{25}$$

where the l and t are the longitudinal and transverse polarizations, ρ is the density, and C_{11} and C_{44} are two of the moduli of elasticity and can be measured from numerical simulations using a technique described by Frenkel and Smit [37]. Based on simulations and using Eq. (23) the propagation speeds in the [1 0 0] direction for LJ solids are

$$c_l = 9.53(\varepsilon/m)^{1/2} \tag{26}$$

$$c_t = 7.20(\varepsilon/m)^{1/2}. \tag{27}$$

A second method for determining the phonon propagation speeds is by generating wavepackets as described by Schelling et al. [32,55] and adjusting the initial velocity in order to obtain a coherent propagating wavepacket. Based on simulations of five different samples the measured speeds are

$$c_l = 9.79 \pm 0.24(\varepsilon/m)^{1/2} \tag{28}$$

$$c_t = 6.47 \pm 0.01(\varepsilon/m)^{1/2}. \tag{29}$$

Substituting Eqs. (28),(29) and (23) into Eq. (22) leads to

$$h_{BD} = 6.72\frac{k_B\left(\frac{\varepsilon_1}{m_1}\right)^{1/2}\left(\frac{m_2}{\varepsilon_2}\right)}{\sigma^3\left(\frac{m_1}{\varepsilon_1}+\frac{m_2}{\varepsilon_2}\right)} \tag{30}$$

or in LJ reduced units

$$h_{BD} = 6.72\frac{\left(\frac{m_2}{\varepsilon_2}\right)}{\left(\frac{m_1}{\varepsilon_1}+\frac{m_2}{\varepsilon_2}\right)}. \tag{31}$$

The difference in the theoretical h_{BD} when using the speeds defined by Eqs. (26) and (27) versus Eqs. (28) and (29) is less than 6%.

The theoretical h_{BD} values are plotted versus different Debye temperature ratios in Fig. 4 for a temperature of 0.25. The DMM under the Debye approximation fits the h_{BD} values for highly mismatched materials fairly well, but tends to underpredict conductance for low-mismatch interfaces by as much as a factor of two in the case of $m_1 : m_2 = 2 : 1$. This discrepancy between DMM and simulated data for highly matched interfaces is due the definition of temperature assumed by the DMM. It was pointed out by Simons [56] and later discussed in more detail by Katerberg et al. [57], that the mismatch models assume the phonon distributions on both sides of the interface to be at equilibrium and their distribution to follow the Bose–Einstein distribution. However, in the case of the NEMD measurements made in this study, temperature is measured in the interface region. The NEMD temperature contains information about waves coming deep within either side of the interface, so that for the case of large temperature gradients in the materials, the equilibrium approximation becomes less valid. Again, this is only an issue for highly matched interfaces.

3.1.2. Measured density of state and propagation speeds

An alternative to the Debye approximation is to directly measure the vibrational DOS in MDS. The occupied vibrational states are determined by conducting a Fourier-transform of the atomic velocity autocorrelation function [58,59]. The general expression for the velocity autocorrelation function is

$$VAF(\tau) = VAF(l\Delta t) = \frac{1}{k}\sum_{i=1}^{k}(\vec{V}_i(t=t_0)\cdot\vec{V}_i(t=t_0+l\Delta t)) \tag{32}$$

where τ, l, k, $\vec{V}_i$, t_0, and Δt are autocorrelation time, a positive integer, the number of atoms in the region of interest, velocity of atom i in the region of interest, starting time in

the calculation of the autocorrelation function, and time step of simulation, respectively.

The measured DOS for four LJ solids with the four different masses used in this study are shown in Fig. 5. The angular frequency is in reduced units, which is why the DOS values line up with one another. In addition to changing the masses, the DOS were also calculated at several different temperatures to verify that $g(\omega)$ was in fact not a function of temperature.

The spectra can be scaled under the harmonic approximation by noting that the energy per unit volume of a subsystem can be expressed as

$$u_{\text{total}} = \int_0^{\omega_{\max}} g(\omega) n(\omega, T) \hbar\omega \, \mathrm{d}\omega = \int_0^{\omega_{\max}} C g'(\omega) T \hbar\omega \, \mathrm{d}\omega = 3 n k_{\mathrm{B}} T \tag{33}$$

where $g(\omega)n(\omega, T)$ can be expressed as $Cg'(\omega)T$ in the MD case and where C is the scaling factor, and $g'(\omega)$ is the unscaled spectrum. This technique does not separate the phonon spectra into individual polarizations. The wave propagation speed is determined by generating wavepackets as mentioned above. Because the DOS is not separated into polarizations, an effective velocity must be used, which can be defined by

$$c_{\text{eff}} = \frac{2c_{\text{t}} + c_{\text{l}}}{3}. \tag{34}$$

This effective velocity definition is chosen so that Eq. (15) will give equivalent results under the Debye approximation regardless of whether the wave speeds are treated separately for each polarization or as an effective polarization for a transmission coefficient of one. Eq. (15) simplifies with the use of Eqs. (28), (29), (33) and (34), and, in reduced units form, is given by

$$h_{\mathrm{BD},1} = 6.72 \frac{\int_0^{\varpi_{\max}} g'_{1,j}(\omega) \omega a(\omega) \, \mathrm{d}\omega}{\int_0^{\varpi_{\max}} g'_{1,j}(\omega) \omega \, \mathrm{d}\omega}. \tag{35}$$

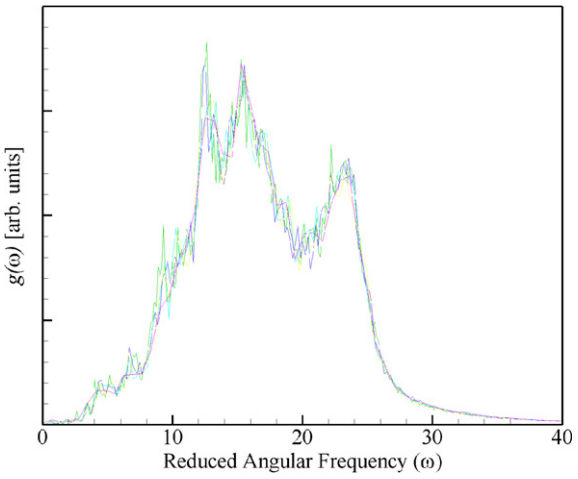

Fig. 5. Unscaled density of vibrational states for four LJ solids with different masses.

The transmission coefficient, $\alpha(\omega)$, for the DMM can be determined by numerically solving Eq. (15) using the measured density of states and the effective velocity defined by Eq. (34).

Theoretical h_{BD} values based on the measured DOS are plotted versus different Debye temperature ratios in Fig. 4 for a temperature of 0.25. The ratios of h_{BD} predicted in NEMD to the theoretical values obtained with a calculated DOS are also plotted. As in the Debye approximation method, the theoretical model appears to work relatively well for highly mismatched surfaces, but underpredicts conductance for interfaces with similar materials by nearly a factor of two. This trend differs from that observed experimentally for real interfaces by Stevens et al. [60] and Stoner and Maris [21], where measured conductances were below the DMM theoretical values. It should be noted that the NEMD simulations are for atomically perfect interfaces, while the real samples are likely to contain interfaces that are not atomically perfect. The difference in the trends between the NEMD approach and experiments on real interfaces may also be due to the choice of the LJ potential.

3.2. Temperature dependence

Although the DMM using the Debye approximation or measured vibrational DOS appears to work well for highly mismatched materials at a temperature of 0.25, it turns out h_{BD} is highly temperature dependent. In the classical high temperature limit, h_{BD} calculated by either the DMM and AMM is independent of temperature. The only temperature dependent part of both models is associated with the distribution function. For these models, at temperatures well above the Debye temperature h_{BD} becomes constant. Because the models do not assume any inelastic scattering, the transmission coefficient is not dependent on temperature. To check whether h_{BD} is dependent on temperature, several simulations were conducted at five temperatures ranging from 0.08 to 0.42. The simulations were conducted on both a highly and a slightly mismatched interface with Debye temperature ratios of 0.2 and 0.5. The temperature dependence of h_{BD} is shown in Fig. 6, which shows a strong linear relationship with h_{BD} varying by nearly a factor of four for both interfaces in the temperature range considered. To give a better intuitive sense of the temperature range considered, recall that the melting temperature for LJ solids is about $T = 0.5$.

The strong linear dependence indicates that there is some thermal transport mechanism that is dependent on temperature, which leads to a larger transmission coefficient. The most likely explanation for this discrepancy is that the DMM accounts only for the elastic scattering, while NEMD accounts for both elastic and inelastic scattering at the interface. The linear temperature dependence indicates a scattering process that is proportional to phonon population, since the phonon population increases linearly with temperature at high temperatures. In the

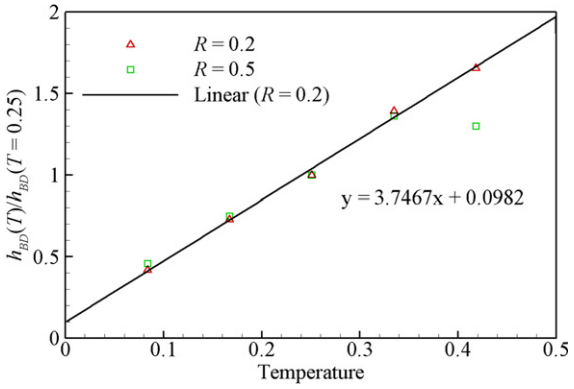

Fig. 6. h_{BD} dependence on temperature for Debye temperature mismatch ratios of 0.2 and 0.5. Data are normalized to the value of h_{BD} at $T = 0.25$.

classical limit and for LJ potential interfaces at temperatures above the Debye temperature, it appears that inelastic scattering provides the major contribution to the energy transport across the interface, surpassing the contribution of the elastic scattering. Based on these results a more suitable model for thermal transport across interfaces in the classical limit is

$$q'' = (h_{BD,E} + h_{BD,I}(T))\Delta T \tag{36}$$

where $h_{BD,E}$ and $h_{BD,I}(T)$ are the interface thermal conductance terms associated with elastic and inelastic scattering and $h_{BD,I}$ is a linear function of temperature. For LJ potential interfaces, inelastic scattering appears to play a critical role in interface thermal transport. The degree to which inelastic scattering influences thermal transport for other atomic potentials may vary. The increase in thermal boundary conductance with temperature has recently been reported experimentally by Lyeo and Cahill [61] and Hopkins et al. [62].

At temperatures above 0.35, the sample with a large Debye temperature ratio had a leveling off in the measured h_{BD}. At first, it was believed to be some error in the simulation, but a second simulation under the same conditions but with different initial velocity distributions of the atomic system resulted in the same lower than expected h_{BD} within the uncertainty of simulation. This drop off could be due to the saturation in transport mechanisms for matched interfaces.

4. Interface defects

The impact of the vibrational DOS and temperature on interfacial thermal transport for atomically perfect interfaces was considered above. Although the analysis of the atomically perfect interfaces provides useful insights into the mechanisms of the thermal transport, the interfaces in real materials are seldom atomically perfect. Most of the reported computational studies, including both lattice and molecular dynamics simulations have only considered atomically perfect interfaces [24,32,51,63]. Early experimental and theoretical work performed for low temperatures of liquid–solid interfaces found that interfacial defects could have a dramatic influence on thermal transport. Weber et al. found that a "perfect interface" made by cleaving LiF and NaF crystals in liquid helium resulted in reduced phonon transport across the interface compared to earlier measurements on non-perfect interfaces [64]. The reduced h_{BD} is often attributed to the loss of phonon coupling on both sides of the interface because localized interface states are removed. On the other hand, Pohl and Stritzker found that, for Au–sapphire interfaces, roughened interfaces resulted in a decrease in h_{BD} at low temperatures [65]. Like the experimental work, computational models have shown that defects and varying interface conditions can lead to either increase or decrease in the thermal boundary resistance [25,27,28,31,34]. This section examines the impact large lattice mismatches, interface mixing, and vacancies have on the thermal transport at LJ interfaces.

4.1. Defects introduced by large lattice mismatches

To mimic defects associated with large lattice mismatches, an interface was created with a lattice mismatch ratio of $\sigma_A/\sigma_B = 0.833$. Side A of the system had $6 \times 6 \times 20$ unit cells and side B had $5 \times 5 \times 20$ unit cells. The ends were subject to the rigid wall conditions. The entire sample was heated to slightly above melting ($T > 0.5$) for a time of 115. The sample was then quenched for a time of 115 resulting in the formation of a thin disordered layer at the interface, which were only a few atomic layers thick. Simulations were then conducted on this interface in a similar fashion as those for the mass mismatch series described earlier.

As can be seen in Fig. 7, h_{BD} values for the small Debye temperature ratios obtained for the disordered interface are

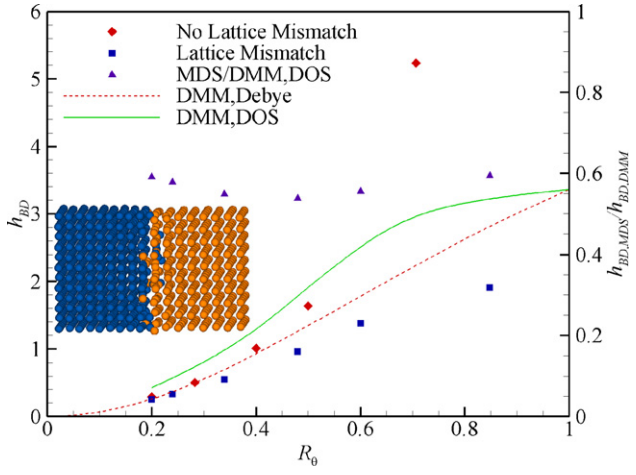

Fig. 7. h_{BD} versus Debye temperature ratio for interfaces with a LJ lattice parameter mismatch ratio of 6:5 (squares) and no lattice mismatch (diamonds). Also included are the DMM predictions based on the simulated DOS and the Debye model. The inset is a portion of the interface after being subjected to a heat treatment and then quenched.

comparable to the results obtained for the atomically perfect interfaces. However, as the Debye temperature ratio increases and approaches a well matched interface, h_{BD} begins to plateau and deviate from the results obtained for atomically perfect interfaces. The results shown in Fig. 7 clearly indicate that the presence of defects at the interface has the greatest impact on thermal transport for interfaces with small frequency mismatched materials. These results differ slightly from those reported by Petterson and Mahan, where they found a significant reduction in h_{BD} regardless of Debye temperature mismatch for lattice mismatched interfaces. They used lattice-dynamic simulations that were restricted to elastic scattering (harmonic model) and very ordered interfaces [25]. Petterson and Mahan modeled interfaces that had perfect crystal structures on both sides of the interface without allowing for a structural relaxation.

The small difference between the results obtained for the disordered and atomically perfect interfaces in the simulations performed for high mass mismatches (small R_θ) is most likely related to almost complete scattering of phonons incident on the interface. Although the added defects at the interface will result in an increase in scattering at the interface, the defects do provide an increased opportunity for inelastic scattering to occur for the highly mismatched interfaces. In the case of highly matched interfaces, the defects increase scattering sites adding thermal resistance to the interface. Similar trends were found in simulations using a lattice mismatch ratio of 4:5.

Also included in Fig. 7 are the DMM predictions of h_{BD} using both the simulated DOS and the Debye model for DOS. The DMM fits the data obtained for the defected interface better than the ones from the atomically perfect interface simulations. This is reasonable considering that the primary assumption made in the DMM is the complete diffuse scattering at the interface. The added defects due to a large lattice mismatch appear to ensure complete scattering. Interestingly, the ratio of simulated h_{BD} to the DMM h_{BD} using the measured DOS is between 0.54 and 0.60 for all interfaces simulated with large lattice mismatches. If the same h_{BD} – temperature relationship exists as described above, than the DMM would be an excellent fit for most simulated data at a temperature of ~0.45.

4.2. Interface mixing and other defects

Often an interface between two materials consists of a region where atoms from either side of the interface diffuse into the other side or even form a compound, as is the case for silicides. In particular, silicide layers can be found at Pt–Si and Cr–Si interfaces. The impact of the interface mixing on thermal transport was considered by Kechrakos [26]. Kechrakos used a lattice dynamics approach and found that, for highly mismatched materials, interface mixing improved thermal transport by as much as a factor of three. Twu and Ho considered interatomic mixing using a NEMD technique for interfaces between parts of the system described by LJ and Morse interatomic potential [34]. They found a reduction in the thermal conductance of nearly a factor of two for one particular interface.

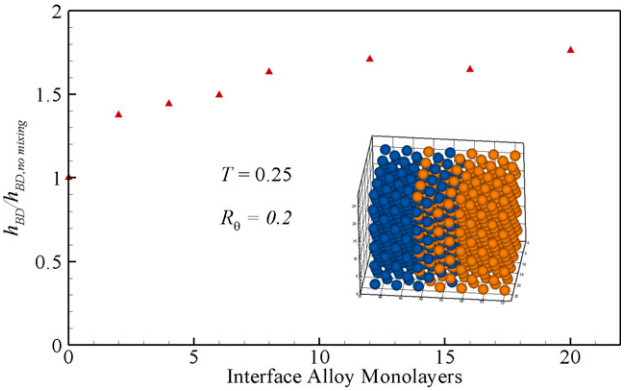

Fig. 8. h_{BD} versus interface alloying thickness. h_{BD} is normalized to the value of h_{BD} obtained in a simulation with no alloying. An atomic-level structure of an interface with four atomic planes mixed is shown in the inset.

To investigate the impact of LJ interface mixing on h_{BD} values, a series of simulations was conducted at $T = 0.25$ and $R_\theta = 0.2$. Different degrees of mixing were simulated by systematically mixing atoms in 2, 4, 6, 8, 12, 16, and 20 atomic planes. As seen in Fig. 8, h_{BD} for mixed interfaces are as much as a factor of 1.8 higher than those for atomically perfect interfaces. This increase for highly mismatched interfaces is most likely due to an increase in scattering sites and localized interface vibrational states that bridge the two different vibrational DOS on either side of the interface.

Simulations were also conducted for single edge dislocations per crystal, resulting in a 10% vacancy density. The changes in h_{BD} were less than the uncertainty in the measurement. The same result was found for point vacancies at a density of 1%, indicating that minor defects have little impact on the overall interface thermal transport for LJ solids.

5. Conclusions

A complete understanding of the thermal transport at solid–solid interfaces at room temperatures is becoming increasingly important with the growing interest in nanoscale technologies. Suitable models of interfacial transport would open the doors for designing engineering materials with specific thermal properties as well as providing us with the tools required to deal with thermal issues that will be a part of tomorrow's technologies. To better the understanding of interface thermal transport, this study uses nonequilbrium molecular dynamics simulations to measure thermal transport for a range of Lennard-Jones interfaces. Initially, simulations were conducted on atomically perfect interfaces for a range of mass mismatched materials. By changing the mass ratio across the interface, the respective

vibrational states can be changed. For these ideal cases, the interfacial conductance decreased with increasing mismatch, as expected. The DMM appears to fit the NEMD results well for poorly matched interfaces at a temperature of 0.25 in LJ reduced units, but it underpredicts conductance for highly matched interfaces. This discrepancy between the DMM and NEMD results is most likely due to the assumption made that the temperature on one side of the interface is strictly due to the phonons incident on the interface, while the MDS temperature is based on all vibrations including those traveling to and from the interface. This result was predicted by Simons [56] and discussed by Katerberg [57]. In addition, the DMM assumption of the complete diffuse scattering at the interface is not valid for an atomically perfect interface.

One of the key findings of this study is that there is a significant interfacial thermal transport dependence on temperature for the NEMD LJ interfaces, which is not accounted for by the mismatch models where only elastic scattering is considered. The interface conductance was found to have a linear dependence on temperature, indicating that interfacial transport is directly related to occupancy of vibration states. Therefore, inelastic scattering appears to play a critical role in the interfacial thermal transport. The importance of inelastic scattering may be highly dependent on the interatomic potential chosen, which should be explored in future works.

A relaxation of a system with large lattice mismatch was used to produce a partially disordered interface. In this case, the thermal interfacial conductance dramatically decreased as compared to the atomically perfect interfaces with similar Debye temperatures or density of states. For the case where the Debye temperature ratio was $R_\theta = 0.85$, the decrease in the interfacial thermal transport was more than a factor of four. Large lattice mismatches had minimal impact on thermal transport for highly mass mismatched interfaces. This trend is in agreement with the NEMD data for $R_\theta > 0.5$. Therefore, interface defects must be accounted for when the Debye temperature ratio approaches one, but are negligible for highly mismatched interfaces.

Interface mixing improves thermal transport by nearly a factor of two for mixing depths of 20 atomic planes for highly mismatched interfaces. This may explain some of the additional thermal transport observed in the NEMD data for highly mass mismatched interfaces. However, this does not account for the nearly two orders of magnitude differences between the measured and DMM thermal boundary conductance for highly mismatched interfaces seen by Stoner and Maris [21].

Acknowledgments

Rob Stevens gratefully acknowledges the support of the National Science Foundation through an IGERT Fellowship and the ARCS Foundation, Inc.

References

[1] C.-L. Tien, A. Majumdar, F.M. Gerner (Eds.), Microscale Energy Transport, Taylor & Francis, Washington, DC, 1998.
[2] D.G. Cahill, W.K. Ford, K.E. Goodson, G.D. Mahan, A. Majumdar, H.J. Maris, R. Merlin, S.R. Phillpot, Nanoscale thermal transport, J. Appl. Phys. 93 (2003) 793–818.
[3] R. Venkatasubramanian, E. Siivola, T. Colpitts, B. O'Quinn, Thin-film thermoelectric devices with high room-temperature figures of merit, Nature 413 (2001) 597–602.
[4] D.G. Cahill, A. Bullen, S.-M. Lee, Interface thermal conductance and the thermal conductivity of multilayer thin films, High Temp. High Pressures 32 (2000) 135–142.
[5] G.D. Mahan, L.M. Woods, Multilayer thermionic refrigeration, Phys. Rev. Lett. 80 (1998) 4016–4019.
[6] L.W. da Silva, M. Kaviany, Micro-thermoelectric cooler: interfacial effects on thermal and electrical transport, Int. J. Heat Mass Transfer 47 (2004) 2417–2435.
[7] Z. Xiao, R.L. Zimmerman, L.R. Holland, B. Zheng, C.I. Muntele, D. Ila, Nanoscale BixTe3/Sb2Te3 multilayer thin film materials for reduced thermal conductivity, Nucl. Instr. Methods Phys. Res. B 242 (2006) 201–204.
[8] X.B. Zhao, X.H. Ji, Y.H. Zhang, T.J. Zhu, J.P. Tu, X.B. Zhang, Bismuth telluride nanotubes and the effects on the thermoelectric properties of nanotube-containing nanocomposites, Appl. Phys. Lett. 86 (2005) 062111–062113.
[9] G. Chen, A. Narayanaswamy, C. Dames, Engineering nanoscale phonon and photon transport for direct energy conversion, Superlattices Microstruct. 35 (2004) 161–172.
[10] R. Yang, G. Chen, Thermal conductivity modeling of periodic two-dimensional nanocomposites, Phys. Rev. B 69 (2004) 195316–195325.
[11] C. Dames, M.S. Dresselhaus, G. Chen, Phonon thermal conductivity of superlattice nanowires for thermoelectric applications, MRS 20003 Fall Meeting, vol. 793, Boston, MA, 2004, pp. S1.2.1-6.
[12] P.E. Phelan, Application of diffuse mismatch theory to the prediction of thermal boundary resistance in thin-film high-Tc superconductors, J. Heat Transfer 120 (1998) 37–43.
[13] P.E. Phelan, Y. Song, O. Nakabeppu, K. Ito, K. Hijikata, T. Ohmori, K. Torikoshi, Film/substrate thermal boundary resistance for an Er–Ba–Cu–O high-Tc thin film, J. Heat Transfer 116 (1994) 1038–1041.
[14] M. Nahum, S. Verghese, P.L. Richards, K. Char, Thermal boundary resistance for YBa[sub 2]Cu[sub 3]O[sub 7-delta] films, Appl. Phys. Lett. 59 (1991) 2034–2036.
[15] S. Zeuner, H. Lengfellner, W. Prettl, Thermal boundary resistance and diffusivity for YBa2Cu3O7-delta films, Phys. Rev. B 51 (1995) 11903–11908.
[16] D.G. Cahill, Heat transport in dielectric thin films and at solid–solid interfaces, Microscale Thermophys. Eng. 1 (1997) 85–109.
[17] E.-K. Kim, S.-I. Kwun, S.-M. Lee, H. Seo, J.-G. Yoon, Thermal boundary resistance at Ge2Sb2Te5/ZnS:SiO2 interface, Appl. Phys. Lett. 76 (2000) 3864–3866.
[18] I.M. Khalatnikov, J. Exp. Theoret. Phys. (USSR) 22 (1952) 687.
[19] W.A. Little, The transport of heat between dissimilar solids at low temperatures, Canad. J. Phys. 37 (1959) 334–349.
[20] E.T. Swartz, R.O. Pohl, Thermal resistance at interfaces, Appl. Phys. Lett. 51 (1987) 2200–2202.
[21] R.J. Stoner, H.J. Maris, Kapitza conductance and heat flow between solids at temperatures from 50 to 300 K, Phys. Rev. B 48 (16) (1993) 373–316,387.
[22] R.J. Stevens, A.N. Smith, P.M. Norris, Measurement of thermal boundary conductance of a series of metal–dielectric interfaces by the transient thermoreflectance technique, J. Heat Transfer 127 (2005) 315–322.
[23] E.T. Swartz, R.O. Pohl, Thermal boundary resistance, Rev. Mod. Phys. 61 (1989) 605–668.

[24] D.A. Young, H.J. Maris, Lattice-dynamical calculation of the Kapitza resistance between fcc lattices, Phys. Rev. B 40 (1989) 3685–3693.
[25] S. Pettersson, G.D. Mahan, Theory of the thermal boundary resistance between dissimilar lattices, Phys. Rev. B 42 (1990) 7386–7390.
[26] D. Kechrakos, The role of interface disorder in thermal boundary conductivity between two crystals, J. Phys.: Condens. Matter 3 (1991) 1443–1452.
[27] G. Fagas, A.G. Kozorezov, C.J. Lambert, J.K. Wigmore, Lattice-dynamical calculation of phonon scattering at a disordered interface, Physica B 263–264 (1999) 739–741.
[28] G. Fagas, A.G. Kozorezov, C.J. Lambert, J.K. Wigmore, A. Peacock, A. Poelaert, R.d. Hartog, Lattice dynamics of a disordered solid–solid interface, Phys. Rev. B 60 (1999) 6459–6464.
[29] W.E. Pickett, J.L. Feldman, J. Deppe, Thermal transport across boundaries in diamond structure materials, Modell. Simul. Mater. Sci. Eng. 4 (1996) 409–419.
[30] A. Maiti, G.D. Mahan, S.T. Pantelides, Dynamical simulations of nonequilibrium processes – heat flow and the Kapitza resistance across grain boundaries, Solid State Commun. 102 (1997) 517–521.
[31] B.C. Daly, H.J. Maris, K. Imamura, S. Tamura, Molecular dynamics calculation of the thermal conductivity of superlattices, Phys. Rev. B 66 (2002), 024301, 024301–024307.
[32] P.K. Schelling, S.R. Phillpot, P. Keblinski, Phonon wave-packet dynamics at semiconductor interfaces by molecular-dynamics simulation, Appl. Phys. Lett. 80 (2002) 2484–2486.
[33] X.-G. Liang, L. Sun, Interface structure influence on thermal resistance across double-layered nanofilms, Microscale Thermophys. Eng. 9 (2005) 295–304.
[34] C.-J. Twu, J.-R. Ho, Molecular-dynamics study of energy flow and the Kapitza conductance across an interface with imperfection formed by two dielectric thin films, Phys. Rev. B 67 (2003), 205422, 205421–205428.
[35] S.H. Choi, S. Maruyama, Thermal boundary resistance at an epitaxially perfect interface of thin films, Int. J. Thermal Sci. 44 (2005) 547–558.
[36] P. Chantrenne, J.-L. Barrat, Finite size effects in determination of thermal conductivities: comparing molecular dynamics results with simple models, J. Heat Transfer 126 (2004) 577–585.
[37] D. Frenkel, B. Smit, Understanding Molecular Simulation, Academic Press Inc, San Diego, 1996.
[38] D.A. McQuarrie, Statistical Mechanics, University Science Books, Sausalito, CA, 2000.
[39] P.K. Schelling, S.R. Phillpot, P. Keblinski, Comparison of atomic-level simulation methods for computing thermal conductivity, Phys. Rev. B 65 (2002) 144306.
[40] J.R. Lukes, D.Y. Li, X.-G. Liang, C.-L. Tien, Molecular dynamics study of solid thin-film thermal conductivity, J. Heat Transfer 122 (2000) 536–543.
[41] S. Kotake, S. Wakuri, Molecular dynamics study of heat conduction in solid materials, JSME Int. J. 37 (1994) 103–108.
[42] A.R. Abramson, C.-L. Tien, A. Majumdar, Interface and strain effects on the thermal conductivity of heterostructures: a molecular dynamics study, J. Heat Transfer 124 (2002) 963–970.
[43] C. Oligschleger, J.C. Schön, Simulation of thermal conductivity and heat transport in solids, Phys. Rev. B 59 (1999) 4125–4133.
[44] S.D. Stoddard, J. Ford, Numerical experiments on the stochastic behavior of a Lennard-Jones gas system, Phys. Rev. B 8 (1973) 1504–1512.
[45] M.P. Allen, D.J. Tildesley, Computer Simulation of Liquids, Clarendon Press, Oxford, 1987.
[46] T. Ikeshoji, B. Hafskjold, Non-equilibrium molecular dynamics calculation of heat conduction in liquid and through liquid–gas interface, Mol. Phys. 81 (1994) 251–261.
[47] S. Maruyama, A molecular dynamics simulation of heat conduction in finite length SWNTs, Physica B 323 (2002) 193–195.
[48] D.J. Evans, W.G. Hoover, B.H. Failor, B. Moran, A.J.C. Ladd, Nonequilibrium molecular dynamics via Gauss's principle of least constraint, Phys. Rev. A 28 (1983) 1016–1021.
[49] Berendsen, Molecular dynamics with coupling to an external bath, J. Chem. Phys. 81 (1984) 3684–3690.
[50] J.H. Irving, J.G. Kirkwood, The statistical mechanical theory of transport processes. IV. The equations of hydrodynamics, J. Chem. Phys. 18 (1950) 817–829.
[51] J.-L. Barrat, F. Chiaruttini, Kapitza resistance at the liquid–solid interface, Mol. Phys. 101 (2003) 1605–1610.
[52] D.C. Rapaport, The Art of Molecular Dynamics Simulation, Cambridge University Press, Cambridge, 1995.
[53] R.J. Stevens, Thermal Transport at Room Temperature Solid–Solid Interfaces, University of Virginia, Charlottesville, VA, 2005.
[54] C. Kittel, Introduction to Solid State Physics, seventh ed., Wiley, New York, NY, 1996.
[55] P.K. Schelling, S.R. Phillpot, P. Keblinski, Kapitza conductance and phonon scattering at grain boundaries by simulation, J. Appl. Phys. 95 (2004) 6082–6091.
[56] S. Simons, On the thermal contact resistance between insulators, J. Phys. C 7 (1974) 4048–4052.
[57] J.A. Katerberg, J.C.L. Reynolds, A.C. Anderson, Calculations of the thermal boundary resistance, Phys. Rev. B 16 (1977) 673–679.
[58] L.V. Zhigilei, D. Srivastava, B.J. Garrison, Vibrational dynamics of the CH stretching mode of H-terminated diamond surfaces, Surf. Sci. 374 (1997) 333–344.
[59] S.R. Calvo, P.B. Balbuena, Molecular dynamics studies of phonon spectra in mono- and bimetallic nanoclusters, Surf. Sci. 581 (2005) 213–224.
[60] R.J. Stevens, A.N. Smith, P.M. Norris, A.W. Lichtenberger, Thermal boundary resistance of thin metal films and thermally conductive dielectric materials, in: 2003 ASME International Mechanical Engineering Congress & Exposition, Washington, DC, 2003, pp. 41856, 41851–41857.
[61] H.-K. Lyeo, D.G. Cahill, Thermal conductance of interfaces between highly dissimilar materials, Phys. Rev. B 73 (2006) 144301.
[62] P.E. Hopkins, R.N. Salaway, R.J. Stevens, P.M. Norris, Temperature dependent thermal boundary conductance at Al/Al2O3 and Pt/Al2O3 interfaces, International Journal of Thermophysics (accepted for publication).
[63] H.M. Streib, G. Mahler, Lattice theory of ideal hetero structures: influence of interface models on phonon propagation, Z. Phys. B 65 (1987) 483–490.
[64] J. Weber, W. Sandmann, W. Dietsche, H. Kinder, Absence of anomalous Kapitza conductance on freshly cleaved surfaces, Phys. Rev. Lett. 40 (1978) 1469–1471.
[65] R.O. Pohl, B. Stritzker, Phonon scattering at crystal surfaces, Phys. Rev. B 25 (1982) 3608–3614.